Regulating the redox cycle of nickel species for efficient seawater electrolysis

Menghui Qi [a], Minkai Qin [a], Hao Wang [a], Binbin Lin [a], Jiadong Chen [b], Xiaoyun Shi [a],
Xiangbowen Du [a], Shanjun Mao [a], Jingpeng Zhao [c], Hao Zhang [d,*], Lingling Xi [a,*], Yong Wang [a,*]

[a] *Advanced Materials and Catalysis Group, Institute of Catalysis, Department of Chemistry, Zhejiang University, Hangzhou 310058, PR China*
[b] *College of Physics and Optoelectronic Engineering, Shenzhen University, Shenzhen 518060, PR China*
[c] *Quantum Design (Beijing) Co., Ltd, Beijing, China*
[d] *Chemistry Research Laboratory, Department of Chemistry, University of Oxford, Oxford OX1 3TA, UK*

A R T I C L E I N F O

A B S T R A C T

Promoting the self-reconstruction of NiFe-based catalysts represents a promising approach to facilitate seawater splitting, albeit with significant challenges. Herein, the redox cycle of Ni species is subtly regulated by decorating NiFe hydroxides with vanadium. Both experimental and theoretical studies demonstrate that the incorporation of V boosts the self-reconstruction of NiFe hydroxides and allows a superior OER performance on account of diminished propensity for chlorine adsorption and optimized binding energy of oxygen-containing intermediates. Consequently, the NiFeV/NF catalyst delivers 2.0 A cm^{-2} at an ultralow overpotential of 369 mV in 1.0 M KOH and exhibits exceptional stability for 720 h at 20 A in an alkaline membrane electrode assembly (MEA) electrolyzer. In alkaline seawater, it achieves prolonged stability, surpassing 240 h at 500 mA cm^{-2} with OER selectivity of 99 %. This work significantly advances the field of seawater electrolysis powered by marine renewables, paving the way for on-site hydrogen production.

1. Introduction

Electrolyzing water to generate green hydrogen fuel using intermittent solar and wind energy is a highly desirable approach to achieve net-zero emissions and enhance energy utilization [1,2]. Significant advancements have been made in commercial alkaline electrolyzers and proton exchange membrane (PEM)-based electrolyzers that employ high-purity water as feedstock [3–5]. However, the uneven distribution of fresh water resources and scarcity of this valuable and shortage water impose limitations on large-scale hydrogen production reliant on high-purity freshwater [6]. Additionally, the energy-intensive nature of seawater purification system raises operational costs [7]. Direct electrolysis of readily available and economical viable seawater offers a promising solution to these challenges, presenting a practical avenue for sustainable hydrogen production [8,9].

Direct seawater electrolysis lags behind the progress seen in electrolyzing pure water [9–11]. Several challenges are encountered in seawater electrolysis, with one significant issue being the unwanted competing chlorine evolution reaction (CER) [11,12]. This concern can

be addressed by reducing the onset potential of the oxygen evolution reaction (OER) to minimize chlorine generation, considering that the equilibrium potential of CER remains pH-independent [11]. Additionally, hypochlorite formation overpotential in alkaline conditions is approximately 480 mV higher than that of OER, underscoring the need to develop anode catalysts with minimal overpotentials at industrial-level current densities (above 500 mA cm^{-2}) [12]. Another obstacle faced by OER catalysts is their limited durability, predominantly affected by corrosive chloride anions that can compromise the effectiveness of the OER [13]. Hence, there is a compelling need to explore highly active and robust electrocatalysts to enable large-scale hydrogen production from seawater.

Despite notable advancements in the engineered design of noble-metal-base materials (such as Ir and Ru), their significant catalytic prowess in seawater electrolysis is hindered by their scarcity and limited durability, impeding their practical applicability [14–16]. In contrast, economically attractive NiFe-based compounds, encompassing oxides/hydroxides [17–20], sulfides/selenides [17,18,21,22], phosphides/nitrides [23,24], perovskites [25], and molecular complexes [17,

* Corresponding authors.
E-mail addresses: hao.zhang@chem.ox.ac.uk (H. Zhang), xll98731@zju.edu.cn (L. Xi), chemwy@zju.edu.cn (Y. Wang).

26][,] have emerged as promising alternatives to precious metal electrocatalysts, exhibiting remarkable OER performance. Within this range of electrocatalysts, it is widely acknowledged that highly oxidized *in situ*-reconstructed species (such as NiOOH or FeOOH, featuring metal oxidation state exceeding +3) serve as the actual active sites [16,18,20, 23,27–29],. They display superior OER activities through modulation of orbital hybridization between metal d bands and O 2p orbitals, thereby optimizing the bonding energy of oxygen-containing intermediates [30]. However, the sluggish and energy-intensive nature of the reconstruction process, typically involving numerous cyclic voltammetry turns or prolonged periods of high operating voltage [21,31], confines most NiFe-based materials to operate at current densities below 100 mA cm^{-2}. Strategies for material optimization, including sulfur leaching from Fe-NiSOH and the integration of electron-deficient boron into NiFe hydroxides, have demonstrated the ability to expedite reconstruction and enhance OER activity [32,33]. Despite these promising developments, the industrial-grade seawater oxidation still necessitates a high voltage, triggering the undesired competing chlorine evolution reaction (CER) and destabilizing the catalyst structure. Consequently, the pursuit of an effective means to facilitate the self-reconfiguration process of NiFe-based catalysts remains both highly desirable and challenging, aiming to elevate the seawater oxidation activity to the next level.

In this work, we present a compelling demonstration of how the redox cycle of nickel species can be effectively modulated through the incorporation of variable-valence V into NiFe hydroxides. Comprehensive insights obtained from *in-situ* characterization highlight the role of V doping in expediting the conversion of Ni^{2+} to Ni$^{3+\delta}$, thereby facilitating the efficient formation of highly active NiOOH species. Concurrently, the introduction of V serves as both structural and electronic modulator, promoting defect generation and enriching high-valence Ni and Fe species. Molecular probe experiments further validate the suitable OH* adsorption capacity of NiFeV/NF, coupled with a viable subsequent deprotonation process. Finite element analysis (FEA) and density functional theory (DFT) calculations jointly elucidate the ability of NiFeV/NF to mitigate chloride ion aggregation at the anode. Moreover, they reveal an elevated Cl* formation energy barrier of up to 2.04 eV, significantly surpassing the rate-determining step of OER (1.79 eV). Leveraging these advantageous attributes, the NiFeV/NF catalyst demonstrates ampere-level current density output at a notably low overpotential, showcasing its exceptional electrocatalytic performance. Furthermore, the catalyst exhibits remarkable durability, maintaining stability for extended periods of hundreds of hours in both alkaline and alkaline seawater electrolytes. Notably, when employed as the anode material in a membrane electrode assembly (MEA) electrolyzer, the NiFeV/NF catalyst achieves notable hydrogen production rates of 17.3 and 2.0 L h^{-1} in alkaline and alkaline seawater electrolytes, respectively.

2. Experimental

2.1. Materials

Anhydrous ferric chloride (FeCl$_3$), anhydrous vanadium chloride (VCl$_3$), and ruthenium oxide (RuO$_2$) were purchased from Aladdin Chemical Co. Ltd. H$_2^{18}$O (AR, >97 %) was purchased from Macklin. The seawater was collected from the Lingshan Island of Qingdao City in Shandong Province of China (Longitude: 120.181943, Latitude: 35.961482). The purity of nickel foam (NF) is 99.9 % (1 mm, 97 % porosity rate). The water used in all experiments was ultrapure (Millipore, 18.2 MΩ).

All chemicals were purchased from suppliers and used without further purification.

2.2. Synthesis of NiFeV/NF

The NiFeV/NF catalysts was fabricated by an impregnation method. A piece of NF (3 cm × 2 cm × 0.1 cm) was first ultrasonicated in 0.1 M HCl for 20 minutes and then in a mixture of ethanol and water (v/v, 1:1) for 15 minutes. FeCl$_3$ (0.3244 g) and VCl$_3$ (0.2516 g) were dissolved in 20 mL ultrapure water (pH ≈ 2). The cleaned NF was immersed in above solution for 3 minutes and dried in an infrared lamp. The above progress was repeated 3 times. The NF loaded with metal chloride was annealed in a muffle furnace at 250 °C for 2 h with a rate of 5 °C min^{-1} followed by electrochemical activation.

2.3. Synthesis of NiFe/NF and NiV/NF

The NiFe/NF and NiV/NF were obtained by the same approach as the preparation of NiFeV/NF, expect that only FeCl$_3$ (0.3244 g) and VCl$_3$ (0.2516 g) was used.

2.4. Synthesis of RuO$_2$/NF

The resultant loading amount of various catalysts prepared by impregnation method fall within the range of 0.8–1.3 mg cm^{-2}. For comparison purposes, 10 mg RuO$_2$ and 40 μL Nafion solution (5 wt%) were dispersed in 960 μL isopropanol and water (v/v, 1:1) mixed solution, and then sonicated in ice water for 30 minutes to get a homogeneous ink. The 50 μL of the ink was loaded on a treated NF (1 cm × 1 cm) and dried under an infrared lamp.

2.5. Material characterization

The morphologies and dimensions of the catalysts were measured using field-emission scanning electron microscopy (FESEM, Hitachi SU8010). Crystal structures were determined by powder X-ray diffraction (Bruker D8 Advance diffractometer) operating at 40 kV and 30 mA with Cu Kα radiation (λ = 1.5418 Å). The high-resolution Transmission Electron Microscope (HRTEM) was conducted on the JEOL JEM-2100 F at an acceleration voltage of 200 kV. X-ray photoelectron spectroscopy (XPS) analysis was performed on Thermo Scientific ESCALAB 250Xi (Al Kα 1486.6 eV) and the binding energy was calibrated with C 1 s at 284.8 eV. Elemental analysis was detected by NexION 2000 inductively coupled plasma-atomic emission spectrometry (ICP-OES). The gas products during the electrolysis were detected by the on-line gas chromatograph (KeChuang GC 2002). The chloride ion concentration was measured by ion chromatography (Dionex ICS-2000). The Ni and Fe K-edge X-ray absorption fine structure spectra were collected on the Synchrotron Radiation Facility (easyXAFS 300+, easyXAFS, LLC) under transmittance mode. All XAS measurements were carried out at room temperature under ambient pressure. Samples were measured simultaneously in fluorescence mode with metal foils as reference.

2.6. Electrochemical measurements

All the electrochemical measurements were performed using a CHI 760E electrochemical workstation. All the materials were cut into 1 cm × 1 cm and used as the working electrode directly. The Hg/HgO and graphite rod were used as the reference electrode and the counter electrode, respectively. The Hg/HgO electrode was calibrated in a high purity hydrogen saturated electrolyte using Pt plates as the working and counter electrode. The CV curves were scanned at a rate of 1 mV s^{-1}, and the average of the two zero potentials is considered as potential of hydrogen electrode reactions. Herein, 1.0 M KOH (pH = 13.8), alkaline simulated seawater (1.0 M KOH +0.5 M NaCl, pH = 13.8) using ultrapure fresh water as solvent. The alkaline natural seawater (1.0 M KOH + natural seawater, pH = 13.6) solution was prepared by directly replacing the solvent ultrapure water with natural seawater to prepare 1 M KOH solution and then removing the precipitate by filtration. The

catalysts were subjected to cyclic voltammetry (CV) for hundreds of cycles to reach a steady state before routine testing. Linear sweep voltammetry (LSV) curves were recorded from high to low potential with a scan rate of 5 mV s^{-1} without iR-compensation. The double layer capacitance (C_{dl}) was performed in the non-Faradaic potential interval with gradient scan rates. The ECSA was defined as ECSA = C_{dl}/C_s, with C_{dl} representing double-layer capacitance and C_s denoting the specific capacitance of the sample. For this investigation, a standard specific capacitance value of C_s = 0.035 mF cm^{-2} was employed. The roughness factor was determined by dividing ECSA by the geometric surface area of the electrode, which was 1.0 cm^{-2}. *Operando* electrochemical impedance spectroscopy (EIS) was carried out in the frequency range from 10^5 Hz to 10^{-2} Hz at an amplitude of 5 mV. Chronoamperometry curves were recorded at 1.53 V in 1.0 M KOH and chronopotentiometry curves were recorded at 500 mA cm^{-2} in alkaline seawater to study the stability of the catalysts. The methanol oxidation measurements were performed in a rotating ring disk electrode (RRDE, Pine instrument) with the outer Pt ring (0.1866 cm^2) and the inner glass carbon electrode (0.2475 cm^2). The rotational speed fixed at 1600 rpm.

2.7. Faradic efficiency calculation

The faradaic efficiency of different catalysts for the generation of oxygen were tested in two-compartment H-type cell with an anion-exchange membrane (FuMA FAA-3-PK-130) for separating the anode and cathode. The gas was collected after at least 20 min at a different current density and analyzed by gas chromatography. Meanwhile, Argon was constantly purged into the anodic compartment with a flow rate of 10 mL min^{-1}. A thermal conductivity detector (TCD) was used to detect and quantify the generated oxygen.

2.8. Electrochemical measurements in MEA electrolyzer

To construct the membrane electrode assembly (MEA), an 11 × 11 cm^2 anion exchange membrane (Fumasep FAA-3-PK-130) was positioned in the center of a stainless steel plate. Two gaskets were delicately placed on either side, flanking two 10 × 10 cm^2 electrodes (1 mm NF, 97 % porosity rate) of unparalleled craftsmanship. The anode catalyst was composed of NiFeV/NF, while the cathode catalyst was Co/CoO/CoMoO$_3$/NF. The MEA electrolyzer functioned at ambient temperature, with the supply of 1.0 M KOH delivered through a peristaltic pump. When capturing the polarization curve and assessing stability at a current of 20 A, the flow rate was meticulously set at 80 mL min^{-1}. Both the cathode and anode were enveloped in 1000 mL of electrolyte, with the solution replenished every 48 hours under a 20 A current. For seawater electrolysis, the electrode area was changed to 2 × 2 cm^2 and the 1.0 M KOH + natural seawater electrolyte at a temperature of 60 °C was supplied with the flow rate of 40 mL min^{-1}.

2.9. Operando Raman test

The Raman spectra was recorded by LabRAM HR Evolution Raman spectrometer (JY HR800) with an excitation wavelength of 514 nm. The NF-based materials were directly used as working electrode in a home-made electrolytic cell. Raman spectrums at different voltages were collected in 1.0 M KOH and alkaline natural seawater.

2.10. In situ ATR-SEIRAS test

Fourier transform infrared spectra was collected on a Nicolet iS50 FT-IR Spectrometer. The silicon prism was first coated with a gold film by chemical deposition. 2 mg catalyst was dispersed in 1 mL isopropanol and water (v/v, 4:1) mixed solution with 2 vol% Nafion. 20 μL ink was deposited on the gold film. The treated silicon prism, Ag/AgCl electrode and Pt plate serve as the working electrode, reference electrode and counter electrode, respectively. The chronoamperometry measurements

were conducted in 0.1 M KOH under the potential range from 1.1 V to 1.7 V (vs. RHE).

2.11. Operando DEMS measurement

NiFeV samples were subjected to ^{18}O-isotope labeling through a potentiostatic reaction at 1.5 V (vs. RHE) for 30 minutes in a KOH solution with H$_2^{18}$O. Subsequently, the ^{18}O-labeled catalysts underwent several rinses with H$_2^{16}$O to eliminate residual H$_2^{18}$O. DEMS measurements was conducted with a QAS 100 device (Pro-tech Limited Instruments, Shanghai). The ^{18}O-labeled NiFeV served as the working electrode, while Ag/AgCl and Pt wire were utilized as the reference and counter electrodes, respectively. CV measurement was carried out in a KOH solution containing H$_2^{16}$O. Concurrently, the real-time discernment of gaseous products with diverse molecular weights was accomplished via mass spectroscopy.

2.12. DFT calculation

DFT calculations were performed by using the Vienna ab-initio simulation package (VASP). The generalized gradient approximation in the Perdew-Burke-Ernzerhof form was used to describe the exchange and correlation energy. In this work, DFT+U was considered with the U values for Ni, Fe and V, which were U-J = 5.5 eV, 4.3 eV and 3.5 eV, respectively [34,35]. The plane wave basis with an energy cutoff of 400 eV was set to describe the one-electron wave function. The bottom two layers of atoms are fixed to simulate the bulk phase. The (5×5×1) and (1×2×1) Monkhorst-Pack k-points in the Brillouin zone were used for electronic structure analysis and the geometric structure optimization. The atomic positions were fully relaxed until the convergence criteria of residual force was less than 0.02 eV Å^{-1} and the energy difference was < 10^{-5} eV for structural optimizations and total energy calculations of γ-NiOOH (101) surface. A vacuum of 15 Å along z-axis was adopted to avoid neighbor slabs interactions caused by the periodic boundary condition. The van der Waals interaction was considered to incorporate the long-range dispersion effects by implementing DFT-D3 method. The Gibbs free energy for each step involved in the OER was calculated as the following equation:

$$G = E_{DFT} + E_{ZPE} - TS$$

Where E_{DFT} is the ground state total energy, T is the temperature (T = 298.15 K), E_{ZPE} and S are zero-point vibrational energy and entropy, respectively.

For OER, both AEM and LOM mechanism were calculated on Fe, V co-doped γ-NiOOH (101) [36]. The free energy of gaseous O$_2$ is derived as G(O$_2$) = 2 G(H$_2$O) – 2 G(H$_2$) + 4.92 (eV). The CER mechanism follows the reference [37].

2.13. FEA simulation

The COMSOL Multiphysics finite-element-based solver was used to simulate the transport of the hydrated ions and the electric field [38,39]. In this work, the electrical double layer is modelled by the Gouy–Chapman–Stern model, which consists of a Helmholtz layer and a diffusion layer. Combining the 'Electrostatics' with the 'Transport of diluted species' modules to obtain the ions' density in the electrical double layer. The Poisson-Nernst-Planck equations were solved in the diffusion layer at a steady state:

$$\nabla^2 V = \begin{cases} 0 & d < d_H \\ F\sum_i n_i c_i & d > d_H \end{cases}$$

$$\nabla \bullet \left(D_i \nabla c_i + \frac{D_i c_i n_i F}{RT} \nabla V \right) = 0$$

Where d is the distance from the electrode surface into the electrolyte, d_H is the Helmholtz layer's thickness, which can be taken as the radius of the hydroxide ion (0.137 nm) and the thickness of diffusion layer is assumed 100 μm [40,41]. That is, $d < d_H$ within the Helmholtz layer, and $d > d_H$ in the diffusion layer. c_i is the concentration of species i, n_i is the valence of species i, D_i is the diffusion coefficient of species i, R is the ideal gas constant, T is the temperature, F is the faraday constant. In this work, one-dimensional model has been built to represent the nanosheets. Uneven meshes were adopted in the research, in which the mesh element size is 0.66×10^{-9} m near the Helmholtz layer and 0.66×10^{-8} m in the other region. The Butler-Volmer equation was solved to obtain the OER current density:

$$i = i_0 \left[\exp\left(\frac{\alpha_a nF\eta}{RT} \right) - \exp\left(-\frac{\alpha_c nF\eta}{RT} \right) \right]$$

Where α_a, α_c are the dimensionless anodic and cathodic charge transfer coefficients, and n is the number of electrons that the electrode reaction needs, respectively. The Arrhenius law is used to get the exchange current density i_0:

$$i_0 \propto \exp\left(-\frac{E_a}{k_B T} \right)$$

Where k_B is the Boltzmann constant, and E_a (1.82 eV) is the activation energy of the OH^- to O_2 reaction [42].

3. Results and discussion

3.1. Synthesis and structural characterization

The synthesis of NiFeV/NF was carried out through a straightforward impregnation method followed by electrochemical activation (Fig. 1a). The nickel foam (NF) substrate was etched *in situ* using an impregnation solution containing anhydrous ferric chloride ($FeCl_3$) and vanadium trichloride (VCl_3) to form a NiFeV chloride overlayer. After subsequent air calcination and electrochemical activation, the NiFeV chloride overlayer underwent reconstruction and transformation into hydroxide nanoplates. The crystal structures of different samples before and after activation were examined using X-ray diffraction (XRD) (Fig. S1 and Fig. S2). Prior to electrochemical activation, apart from the NF diffraction peaks, the diffraction peaks at 16.1°, 18.4°, and 32.6° were assigned to the (110), (011), and (220) planes of $NiCl_2 \cdot H_2O$ (JCPDS: 01–1260) in both NiFeV/NF and NiFe/NF. However, due to the relatively mild acidity of the impregnation solution containing only VCl_3, the etching process was gentler, resulting in the absence of detectable $NiCl_2 \cdot 6 H_2O$ in NiV/NF. Subsequent XRD analysis of all the activated samples
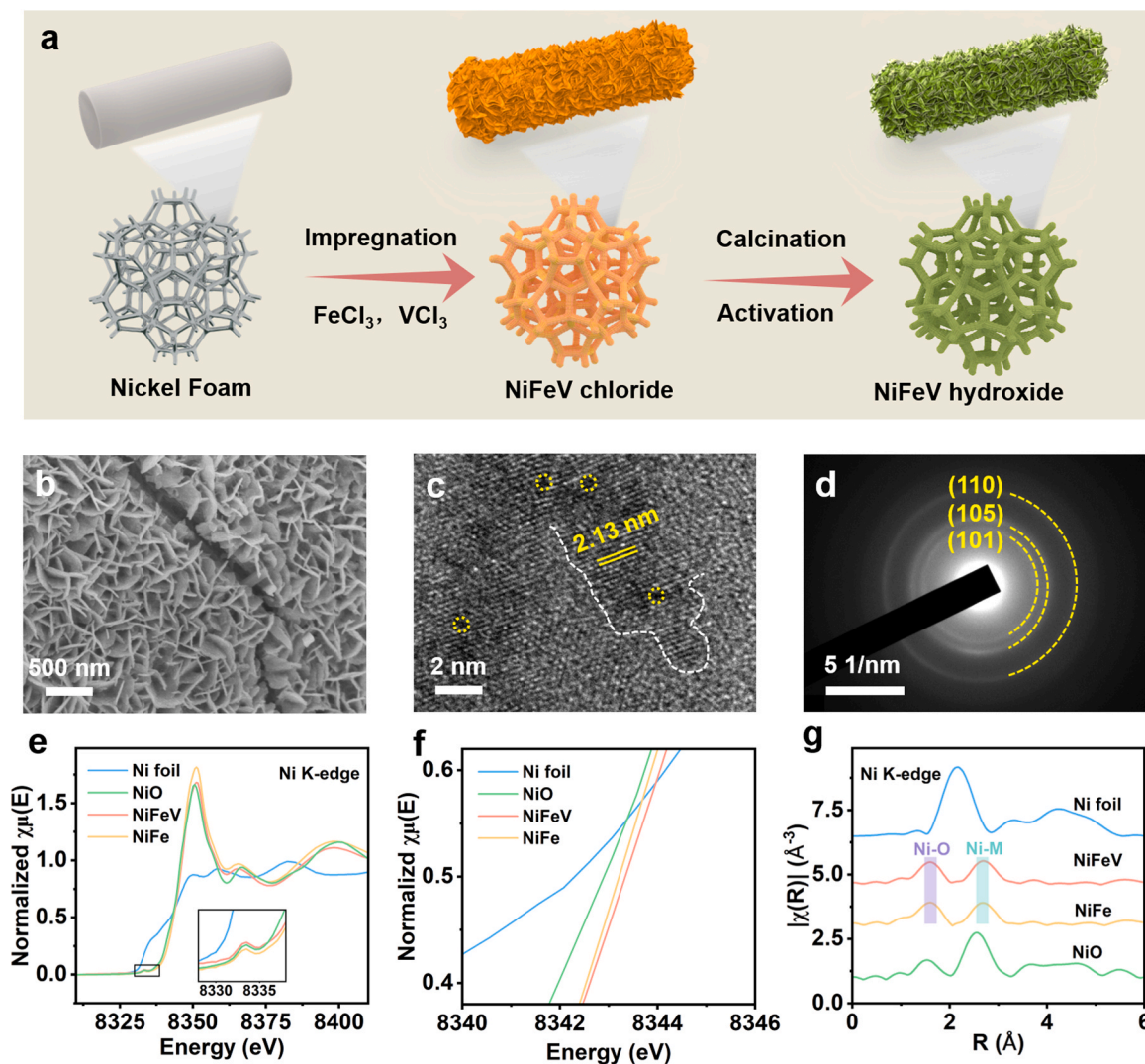

Fig. 1. Structural characterization of NiFeV/NF. (a) Schematic illustration of the synthesis of NiFeV/NF. SEM (b) and HRTEM (c) images of NiFeV/NF. (d) Selected area electron diffraction image of NiFeV/NF. (e) Ni K-edge XANES spectra. (f) A zoom-in XANES spectra. (g) Fourier-transformed k^3-weighted EXAFS spectra.

displayed the peaks corresponding to layered double hydroxide (JCPDS: 38–0715) and NiOOH (JCPDS: 27–0956). As the electrochemical reconfiguration process is confined to the catalyst's surface, the inner core of the catalyst is likely to retain its layered double hydroxide constitution. Scanning electron microscopy (SEM) images showcase the nanoplates morphology of NiFeV/NF embedded within the NF skeleton (Fig. 1**b and** Fig. S3), thereby conferring robust mechanical strength and exceptional electrical conductivity. Conversely, NiFe/NF and NiV/NF display the morphologies of nanofibers and nanoparticles, respectively. Furthermore, high-resolution transmission electron microscopy (HRTEM) was employed for an in-depth examination of the structural features post-activation. HRTEM images reveal the crystallinity of the synthesized nanoplates, albeit with the presence of numerous defects (marked with yellow dashed circles). The measured neighboring inter-layer distance of 0.213 nm concurs with the (105) plane of NiOOH (Fig. 1**c**). The selected area electron diffraction (SAED) image displays several

diffraction rings corresponding to the (101), (105) and (110) lattice planes of NiOOH (Fig. 1**d**) [32]. Additionally, as illustrated in Fig. S4, the thin lamellar structure, composed of a few layers, not only facilitates the exposure of more active sites but also enhances contact with the electrolyte to expedite mass transfer. The corresponding energy dispersive spectroscopy (EDS) elemental maps confirms that the Ni, Fe, and V elements are uniformly distributed over the nanoplates. The content of each metal was quantified through ICP-OES (Table S1). X-ray photoelectron spectroscopy (XPS) was employed to elucidate the elemental chemical states (Fig. S5 **and** Fig. S6). In the case of NiFeV/NF, the high-resolution Ni 2p spectra depict the coexistence of Ni^{2+} and Ni^{3+}. Peaks at 855.5 eV and 873.2 eV correspond to $2p_{1/2}$ and $2p_{3/2}$ of Ni^{2+}, whereas peaks at 857.2 eV and 875.1 eV are attributed to Ni^{3+}, aligning well with previous reports [34]. Comparison with NiFe/NF reveals a shift of Ni^{2+} peaks towards higher binding energy by 0.2 eV upon V introduction, along with an increased peak area ratio of Ni^{3+}, indicating that V doping enhances the electron transfer of Ni and promotes the formation of Ni^{3+} species. The Fe 2p spectra encompass Fe^{2+} peaks at 710.6 eV and 723.5 eV, while the other peaks at 713.0 eV and 725.6 eV are assigned to Fe^{3+} [43]. Notably, the Fe^{3+}/Fe^{2+} area ratio in NiFeV/NF surpasses that of NiFe/NF. In the $V_{2p3/2}$ region, peaks at 515.7, 516.8, and 517.6 eV are attributed to V^{3+}, V^{4+}, and V^{5+}, respectively [35,44]. Remarkably, the proportion of low oxidation state vanadium (V^{3+} and V^{4+}) in NiFeV/NF exceeds that of NiV/NF, substantiating the robust electronic interaction between NiFe and V. Analysis of the O 1 s spectra reveals a decrease in lattice oxygen and an increase in oxygen vacancies in NiFeV/NF, indicative of V's disruptive influence on the ordered atomic arrangement, generating additional unsaturated coordination sites. This not only facilitates the redistribution of local electrons but also modulates the adsorption energy of oxygen intermediates, thereby enhancing the catalytic activity for the OER [45].

X-ray absorption spectroscopy (XAS) was performed to delve deeper into the electronic configuration and coordination characteristics of NiFeV/NF. Specifically, X-ray absorption near edge structure (XANES) at the Ni K-edge of NiFeV/NF demonstrate a higher average oxidation than NiO of +2 (Fig. 1**e and f**). A zoomed-in XANES spectrum unveils subtle blue shift in the absorption energy of the Ni K-edge in NiFeV, which indicate an elevated oxidation state than NiFe counterpart. This observation underscores the substantial impact of V incorporation on the oxidation state, which aligns seamlessly with XPS findings. Intriguingly, the heightened pre-edge peak intensity in NiFeV hints a less centrosymmetric coordination environment for the Ni atoms within NiFeV compared to NiFe [46]. The extended X-ray absorption fine-structure (EXAFS) of NiFeV reveals two dominant peaks at 1.6 Å and 2.7 Å, which are attributed to the Ni-O and Ni-M (M = Ni, Fe, or V) scattering paths, respectively (Fig. 1**g**). Notably, the lower peak intensities corresponding to the Ni-O shell in NiFeV confirm the disruptive influence on the octahedral centrosymmetric structure, setting it apart

from the more symmetric NiFe arrangement. Consistent results are approved using the wavelet transforms (WT) analysis (Fig. S7). This comprehensive XAS investigation substantiates the adjustment of electronic and geometric structure of NiFe hydroxides following incorporation of V.

3.2. OER performance in 1.0 M KOH

The OER performance of the as-prepared catalysts was initially assessed in a 1.0 M KOH solution. The optimization of the Fe and V ratios was conducted as shown in Fig. S8, and the sample co-impregnated with 0.1 M Fe and 0.08 M V (referred to as NiFeV/NF) exhibited the most favorable performance. Linear sweep voltammetry (LSV) curves without iR compensation are depicted in Fig. 2**a**. Notably, NiFeV/NF demonstrated the superior OER activity, requiring only a 263 mV overpotential to achieve a current density of 100 mA cm^{-2}. This stands in comparison to NiFe/NF (272 mV), NiV/NF (344 mV), as well as commercial RuO_2 loaded on NF (376 mV) (Fig. 2**b**). Particularly noteworthy is that at elevated current densities of 500 mA cm^{-2} and 1000 mA cm^{-2}, the requisite overpotential are impressively low at 298 mV and 325 mV, respectively. In contrast, the commercial RuO_2 loaded NF necessitates notably higher overpotentials (463 mV @500 mA cm^{-2} and 526 mV @1000 mA cm^{-2}).

Tafel slopes were calculated to delve further into the OER kinetics of these electrocatalysts. Among the electrocatalysts, the optimal NiFeV/NF catalyst exhibited the lowest Tafel slope of 33 mV dec^{-1}, in comparison to NiFe/NF (40 mV dec^{-1}), NiV/NF (67 mV dec^{-1}), and commercial RuO_2 (100 mV dec^{-1}). This notably reduced Tafel slope signifies enhanced OER reaction kinetics (Fig. 2**c**). Electrochemical impedance spectroscopy (EIS) measurements were also conducted to assess the charge transfer resistance R_{ct} [47]. The equivalent circuit and fitted Nyquist plots are displayed in Fig. S9 and Fig. 2**d**. Remarkably, NiFeV/NF demonstrated a quite low R_{ct} of 0.16 Ω, constituting only 57 % of NiFe/NF and 2.6 % of NiV/NF, providing further evidence of its rapid charge transfer capability. At a potential of 1.53 V (vs. RHE), the O_2 production rate reached ~1.85 mL min^{-1} for NiFeV/NF, nearly 14 times that of commercial RuO_2 (Fig. 2**e**). Furthermore, the Faradaic efficiency of O_2 evolution from NiFeV/NF was examined in a gas-tight H-typed electrochemical cell, separated by an anion exchange membrane. Notably, the O_2 Faradaic efficiency of NiFeV/NF approached 100 % at a high current density of 500 mA cm^{-2} (Fig. 2**f**). Additionally, the long-time stability of NiFeV/NF in OER was assessed using chronoamperometry. Following a 500 h test, the decay in OER activity was negligible, highlighting its remarkable stability (Fig. 2**g**). Furthermore, the robust nanoplate structure of NiFeV/NF was confirmed by nondestructive characterizations after the OER test (Fig. S10 and Table S2). SEM images and corresponding elemental mapping after the OER test indicated that the nanoplate structure remained intact, with even distribution of metallic elements. The presence of the NiOOH phase was also detected by Raman spectra [32,34]. Moreover, when compared with recently reported electrocatalysts, NiFeV/NF exhibited outstanding OER performance in alkaline fresh water electrolytes (Fig. 2**h** and Table S3).

3.3. OER performance in seawater

Given the ultra-low OER overpotential and its sustained stability at industrial current density in a 1.0 M KOH electrolyte, the OER performance was then evaluated in simulated alkaline seawater (1.0 M KOH + 0.5 M NaCl) and alkaline natural seawater (1.0 M KOH + natural seawater), aiming to explore the potential of NiFeV/NF for seawater electrolysis. Notably, even in the simulated alkaline seawater environment, NiFeV/NF exhibited the most favorable performance among the aforementioned materials (Fig. S11). Specifically, NiFeV/NF achieved substantial current densities of 500 and 1000 mA cm^{-2} at remarkably low overpotentials of 327 and 365 mV, respectively. These values are
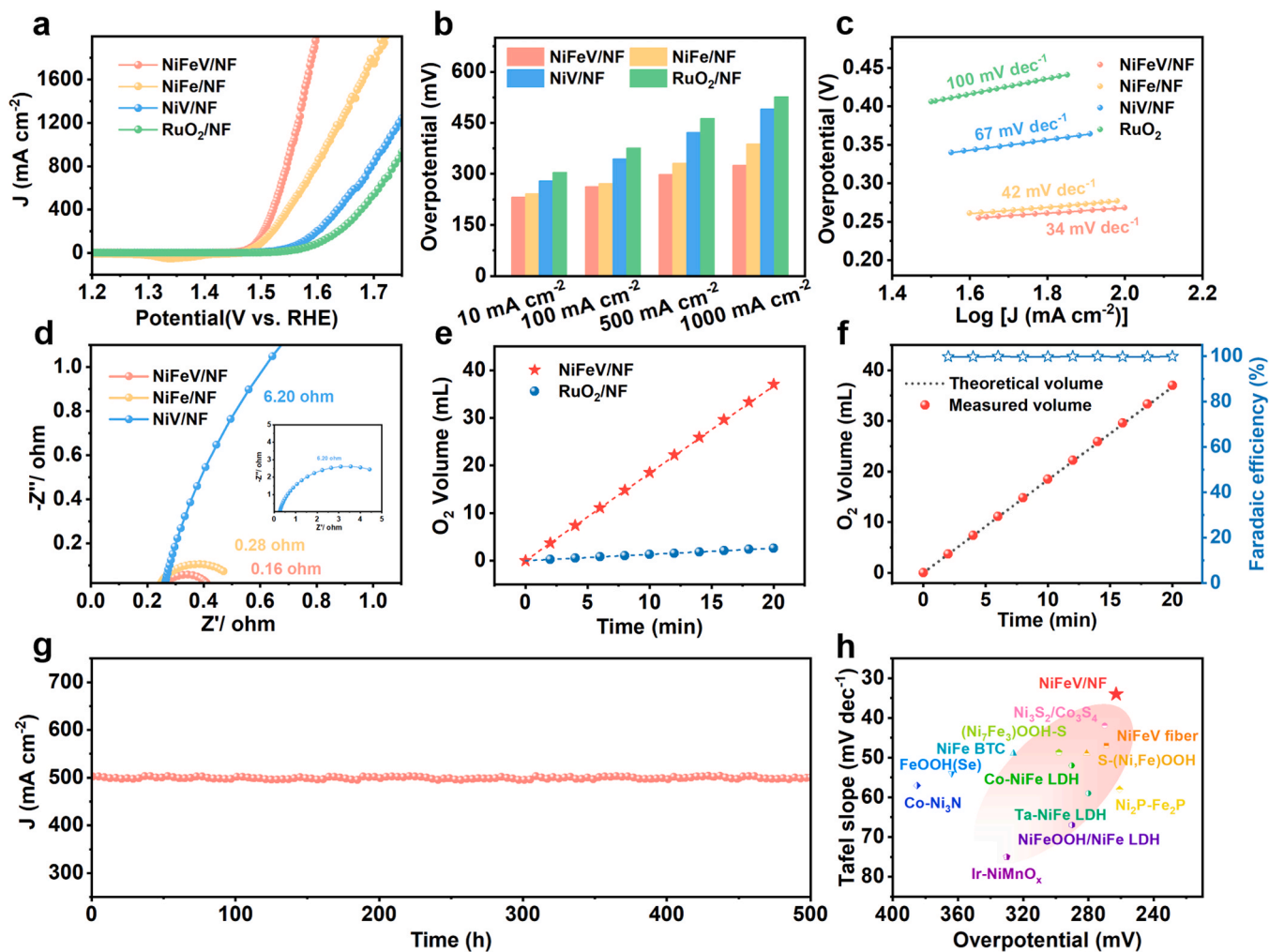
Fig. 2. Electrochemical OER performance in 1.0 M KOH. (a) Linear sweep voltammetry curves of different catalysts without iR compensation. (b) The overpotential comparison at the current density of 10, 100, 500, 1000 mA cm^{-2}. (c) Tafel plots. (d) Nyquist plots measured at 1.5 V (vs. RHE). (e) O$_2$ production for NiFeV/NF and commercial RuO$_2$ at 1.53 V (vs. RHE). (f) Faradaic efficiency measured for NiFeV/NF in H-typed cell at the current density of 500 mA cm^{-2}. (g) Chronoamperometry curve at a constant overpotential of 300 mV. (h) The comparison of the OER performance at 100 mA cm^{-2} and Tafel slopes between NiFeV/NF and other state-of-the-art OER catalysts.

significantly below 480 mV threshold required to initiate the chlorine evolution reaction (CER) [11]. Additionally, NiFeV/NF displayed the lowest Tafel slope and impedance values. The stability evaluation further confirmed the robustness of NiFeV/NF. In a continuous test, NiFeV/NF sustained a current density of 500 mA cm^{-2} at 1.55 V (vs. RHE) for 100 h, demonstrating excellent durability without any noticeable voltage increase. This underscores the remarkable stability of NiFeV/NF as a promising anode material with considerable potential for practical applications.

Electrocatalytic measurements were extended to the context of alkaline natural seawater. The OER activities of the investigated materials exhibited a decline compared to the performance observed in the other two electrolytes. Despite this, NiFeV/NF demonstrated a remarkably low overpotential requirement of 330 mV at 500 mA cm^{-2}. Notably, NiFeV/NF showcased an exceptional current density output of 1.5 A cm^{-2} at an overpotential of 472 mV. This performance surpassed that of NiFe/NF by 1.7 times, NiV/NF by 5.8 times, and RuO$_2$/NF by 11.8 times (Fig. 3a). The Tafel slope for NiFeV/NF was notably shallow at 43 mV dec^{-1} (Fig. 3b), indicative of rapid OER kinetics. Detailed analysis (Figs. S12-S14) revealed that the double-layer capacitance (C$_{dl}$) of NiFeV/NF was comparable to the contrast samples. However, the electrochemical resistance value of NiFeV/NF was the lowest, signifying an enhanced electron transfer rate beneficial for improving OER

efficiency (Fig. S15). Additionally, the Faradic efficiency (FE) was assessed using gas chromatography (GC), with results presented in Fig. 3c and Fig. S16. The GC spectra indicated a remarkable ~99 % oxygen selectivity at 500 mA cm^{-2} for NiFeV/NF. In contrast, RuO$_2$ exhibited only 20 % selectivity to O$_2$, much lower than that of NiFe/NF (96 %) and NiV/NF (92 %). Impressively, even at the current density of 1.0 A cm^{-2}, the peak area of O$_2$ on NiFeV/NF in alkaline natural seawater closely resembled that in the 1.0 M KOH electrolyte (Fig. 3d), further affirming the excellent OER selectivity.

To demonstrate NiFeV/NF's enhanced suppression of CER, examination of oxidized chloride species was conducted via iodide titration [11,16]. Unlike other cases, the electrolyte for NiFeV/NF retained a colorless transparent appearance after iodide titration, indicating minimal generation of reactive chloride species during the OER process. Conversely, the electrolyte from NiFe/NF and NiV/NF showed a shift to faint yellow, while the electrolyte from RuO$_2$ exhibited a darker yellow hue (Fig. S17). This phenomenon underscores NiFeV/NF's effective inhibition of highly corrosive chlorine species during seawater electrolysis. Stability assessment in alkaline natural seawater through chronopotentiometry measurement demonstrated a slight potential increase of 23.3 mV after 240 h of durability testing at an industrial current density of 500 mA cm^{-2} (Fig. 3e). In contrast, the potential for RuO$_2$ increased rapidly within a few hours. Even though the elemental
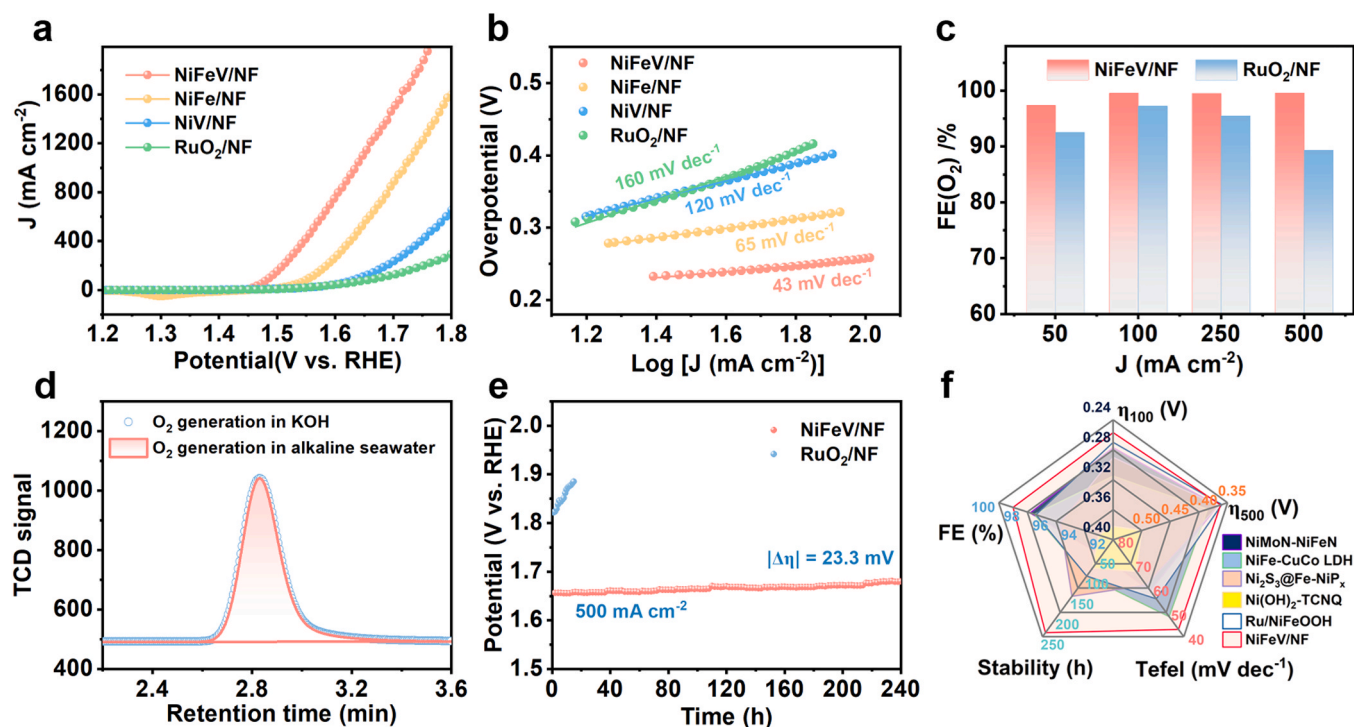
Fig. 3. Electrochemical OER performance in 1.0 M KOH + natural seawater. (a) Linear sweep voltammetry curves of different catalysts without iR compensation. (b) Tafel plots. (c) Faradic efficiency of NiFeV/NF and commercial RuO_2 under different current densities. (d) O_2 yield at the high current density of 1000 mA cm^{-2} obtained by gas chromatography measurements. (e) Durability tests under a constant current density of 500 mA cm^{-2}. (f) Comparison of seawater splitting performance between reported advanced catalysts and NiFeV/NF.

analysis after the reaction showed a slight decrease in the levels of Fe and V metals, TEM images and EDS mapping confirmed that NiFeV/NF maintained its morphology and element distribution even after the stability test (Fig. S18 **and** Table S4). Moreover, NiFeV/NF's electrocatalytic performance surpassed many reported catalysts across various parameters (Fig. 3**f** and Table S5).

3.4. Overall water splitting performance in a MEA device

A home-made MEA electrochemical reactor with dimensions of 10 × 10 cm^2 was employed to assess the practical application potential of our catalyst (Fig. S19 **and** Fig. S20). As depicted in Fig. 4**a**, the anode consisted of NiFeV, while the cathode featured Co/CoO/CoMoO$_3$ (Detailed information regarding the Co/CoO/CoMoO$_3$ cathode is available in our previous report[48]). These components were separated by an anion exchange membrane (Fumasep FAA-3-PK-130, 11 × 11 cm^2). Both the anode and cathode pathways were circulated with a 1.0 M KOH electrolyte using a peristaltic pump, optimized to a flow rate of 80 mL min^{-1}. For comparative purposes, two cleaned commercial nickel foam pieces were employed. A simulated LSV curve was generated by incrementally changing the potential until a steady-state current was reached (Fig. 4**b** and Fig. S21). Notably, the NiFeV || Co/CoO/CoMoO$_3$ configuration required only 1.53 V to achieve a current density of 10 mA cm^{-2}, which was 560 mV lower than that observed for NF || NF (2.09 V). Impressively, the current density soared to 50 A at a mere 3.24 V, suggesting a theoretical production capacity of 22.8 L of green hydrogen per hour. Operating the electrolytic cell at 20 A under 2.30 V yielded stable performance for 30 days, maintaining 97.5 % current retention—a testament to its remarkable stability (Fig. 4**c** and Fig. S22). It is crucial to mention that, while operating continuously at a current of 20 A, the precise testing temperature of the electrolytic cell has been upheld at 33–34 °C (Fig. S23). When compared with NF || NF, this system achieved electricity saving of 1.60 kW·h, 1.83 kW·h, and 1.87 kW·h for the production of per cubic unit of green hydrogen at 5 A,

10 A, and 20 A, respectively (Fig. 4**d and Note 1**).

The practical viability of the catalytic system was further assessed in an alkaline natural seawater environment. A 2 × 2 cm^2 MEA reactor operating at 60 °C was utilized to simulate industrial electrolytic seawater conditions (Fig. S24 **and** Fig. S25). A flow rate of 40 mL min^{-1} was maintained to circulate 1.0 M alkaline natural seawater within the reactor. Notably, the NiFeV || Co/CoO/CoMoO$_3$ configuration exhibited a substantial current density of 0.5 A cm^{-2} prior to the onset of reaction for NF || NF. At an applied voltage of only 3.0 V, a significantly higher current density of 1.13 A cm^{-2} (twice that of NF || NF) was achieved (Fig. 4**e**). Impressively, the cell voltage remained stable when operating under current densities of 0.1 A cm^{-2} and 0.2 A cm^{-2} for a continuous 24-hour period (Fig. 4**f**). Evaluating the stability threshold of the material is a crucial parameter to assess practicality. The cell voltage maintained at 500 mA cm^{-2} for 6 hours even with risk of oxidative etching.

Enhancing the temporal and spatial yield of green hydrogen is of paramount significance for the scalable generation of hydrogen through water splitting. In a 1.0 M KOH electrolyte, the utilization of NiFeV/NF as the anode enables the attainment of a hydrogen production rate reaching 17.3 L h^{-1} at a cell voltage of 2.98 V. This rate is 2.4 times greater than that achieved with commercial NF. Additionally, when powered by just two dry cells (1.5 V each), the seawater splitting cell generates 2 L of hydrogen per hour, aligning well with the capabilities of marine offshore renewable farms for on-site green hydrogen production (Fig. 4**g**) [49]. The aforementioned results further underscore the reliability and promising application potential of NiFeV/NF in alkaline water/seawater electrolysis.

3.5. Mechanistic insight

To establish the structure-activity relationship, *in situ* electrochemical impedance spectroscopy (EIS) was first employed to study the potential-dependent interface behavior during OER. The low-frequency
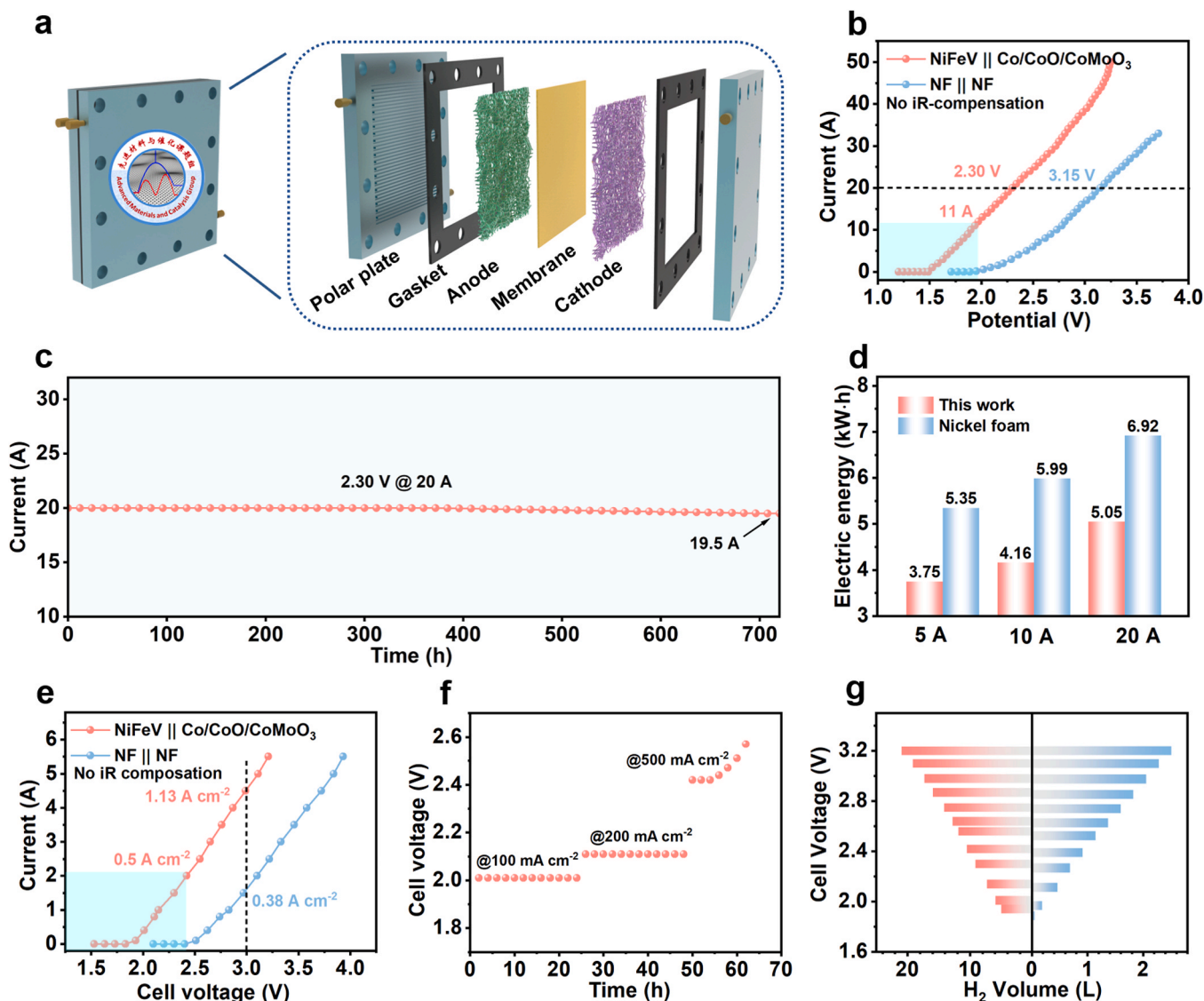
Fig. 4. Membrane electrode assembly reactor for water/seawater oxidation. (a) Schematic illustration of the MEA. (b) The fitting current vs. cell voltage curves for NiFeV || Co/CoO/CoMoO$_3$ and NF || NF in 1.0 M KOH. (c) Long-term stability test under a voltage of 2.30 V without iR compensation in 1.0 M KOH. (d) Comparison of electricity consumption to produce 1 cubic H$_2$ for NiFeV || Co/CoO/CoMoO$_3$ and NF || NF in 1.0 M KOH. (e) The fitting current vs. cell voltage curves for NiFeV || Co/CoO/CoMoO$_3$ and NF || NF in 1.0 M KOH + natural seawater at 60 °C. (f) Durability test for NiFeV || Co/CoO/CoMoO$_3$ in 1.0 M KOH + seawater at 60 °C. (g) Volume of H$_2$ produced per hour in 1.0 M KOH (left) and 1.0 M KOH + seawater (right).

region (10^{-2} Hz-10^1 Hz) is indicative of a non-homogeneous charge distribution, reflecting the presence of OER intermediate species at the electrode interface [47]. Conversely, the high-frequency region (10^1 Hz-10^5 Hz) is associated with the electrooxidation of the catalyst. The optimized fitting model and corresponding parameters are depicted in Fig. S9 and Tables S6-S8. The parameters R_p and R_{ct} represent the resistance for catalyst inner oxidation and interface oxidation reaction, respectively. As illustrated in Fig. 5**a** and Fig. S26, the resistance of the reaction in the high-frequency region notably decreases after 1.35 V (vs. RHE), indicating an accelerated catalyst reconfiguration rate prior to OER. Importantly, it's noteworthy that NiFe/NF displays a larger R_p, suggesting a higher resistance to transition into the catalytically active phase compared to other catalysts. Furthermore, the -phase angle and R_{ct} demonstrate a rapid reduction as the bias potential increases for all examined catalysts, indicating that reducing charge transfer resistance is conducive to promoting OER. Despite this, NiV/NF exhibits a significantly higher R_{ct} value compared to the other catalysts, suggesting a hampered OER process. Strikingly, NiFeV/NF boasts the smallest -phase angle and R_{ct} value, underscoring accelerated reaction kinetics in both

surface reconstruction and the OER process.

To further monitor the dynamic surface reconstruction during OER, *operando* Raman spectroscopy was employed to elucidate the interfacial active phase in the low-frequency region of EIS spectra. As depicted in Fig. 5**b**, up to 0.4 V (vs. Ag/AgCl), the NiFeV/NF displays a peak at 457 cm^{-1} attributed to the vibrations of Ni^{II}-O in the crystal, along with another peak at 528 cm^{-1} assigned to Ni^{II}-O in the defective or the disordered Ni(OH)$_2$ [50,51]. The intensity ratio of the peaks at 528 cm^{-1} and 457 cm^{-1} reflects the proportion of defective Ni(OH)$_x$ species, which exceeds 1 (Fig. S27), indicating the presence of abundant defects in NiFeV/NF. Conversely, *operando* Raman results for NiFe/NF and NiV/NF exhibit no conspicuous signals of the signals of the defective or disordered Ni(OH)$_x$ at 528 cm^{-1} (Fig. S28), implying that the co-incorporation of both Fe and V can effectively induce defect formation. Upon further increasing the applied potential to 0.4 V vs. Ag/AgCl and beyond, a pair of peaks at 477 cm^{-1} and 557 cm^{-1} emerges in the NiFeV/NF electrode, corresponding to γ-NiOOH [52,53]. Moreover, the transformation of Ni^{2+}(OH)$_2$ → Ni$^{3+\delta}$OOH in the NiFeV/NF leads to the generation of Ni$^{3+\delta}$OOH, which is advantageous for OER and occurs
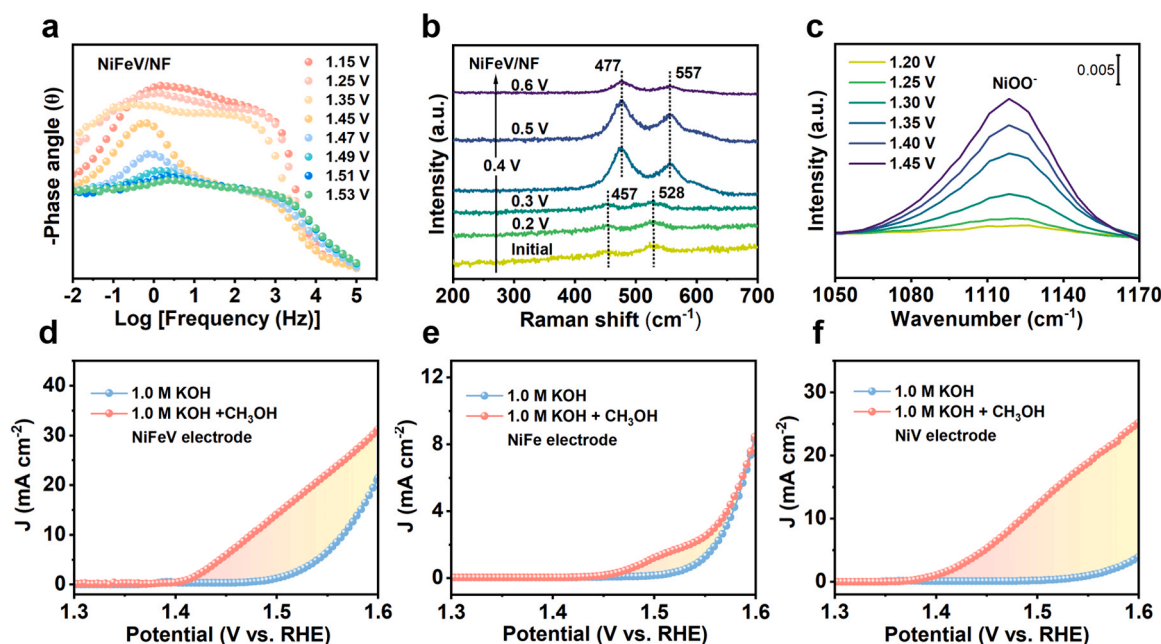
Fig. 5. *Operando* characterizations and surface OH* affinity test. (a) *In situ* Bode phase plots for NiFeV/NF. (b) *Operando* Raman and spectra of NiFeV/NF. (c) *In situ* ATR-SEIRAS spectra of NiFeV/NF. Oxygen intermediates probed via methanol electrooxidation in 1.0 M KOH with and without methanol in different electrodes for (d) NiFeV, (e) NiFe and (f) NiV.

100 mV earlier than in NiFe/NF and NiV/NF. It's worth noting that β-NiOOH also exhibits two Raman bands at positions similar to γ-NiOOH, albeit with a significantly smaller intensity ratio between these two bands [34]. Thus, based on the Raman spectra, the active phases in NiFeV/NF and NiFe/NF are categorized as γ-NiOOH, while the active phase in NiV/NF is identified as β-NiOOH. Furthermore, *in situ* attenuated total reflectance surface-enhanced infrared absorption spectroscopy (ATR-SEIRAS) reveals a broad peak within the range of 1050–1170 cm^{-1} (Fig. 5c), corresponding to the negatively charged "active oxygen" (NiOO$^-$) [54,55], signifying the generation of NiOOH species. These findings robustly indicate that the co-incorporation of Fe and V induces the generation of abundant defects, facilitating the transformation of NiOOH active phases and accelerating the kinetics of the OER.

Investigating the oxygenated intermediates during the OER process is of paramount significance, albeit posing challenging. The adsorption of hydroxyl groups onto a metal surface is regarded as a pivotal initial step in initiating the OER under alkaline conditions [56]. Notably, the electron deficient OH* on the (oxy)hydroxides can be probed using nucleophiles such as methanol molecule [57]. To study this, the rotating ring disk electrode (RRDE) was employed in the methanol oxidation reaction (MOR). Reverse linear scanning voltammetry with a scan rate of 1 mV s^{-1} was adopted to prevent the interference of metal redox peaks. As depicted in Figs. 5d-5f, minimal methanol oxidation currents and negligible current differences resulting from methanol oxidation are observed on the NiFe electrode. The polarization curves in both media rapidly overlap, indicating weaker adsorption ability and a significantly smaller coverage degree of OH*. In contrast, the NiV electrode displays a notable current difference attributed to the electrooxidation of methanol, signifying substantial OH* adsorption on the electrode surface, which is swiftly consumed by methanol molecules. The facile generation of a hydroxyl-rich surface on the NiV electrode also signifies a robust OH* adsorption capacity, thereby complicating subsequent deprotonation steps. A similar yet less pronounced current discrepancy on the NiFeV electrode indicates a moderate OH* binding energy. From these experimental findings, it becomes evident that NiFeV possesses an appropriate hydroxyl adsorption capacity, thereby facilitating the formation of M-OH* and M-O* species, ultimately enhancing OER

performance. Furthermore, the trend of methanol oxidation activity for NiFeV/NF, NiFe/NF, and NiV/NF is in accordance with the RRDE test, except for a two-order magnitude increase in current density (Fig. S29). Thus, the MOR results obtained under the RRDE system genuinely reflect the hydroxyl affinity on the composite foam nickel electrode surface at high current densities.

The wettability of the catalyst surface plays a pivotal role in influencing interfacial reaction kinetics, while the prompt dissipation of bubbles under high current densities contributes to the rejuvenation of the catalyst surface. Consequently, the contact angle test was conducted to assess the hydrophilic characteristics of these catalysts. As illustrated in Fig. S30, the hydrophilicity of NiFeV/NF surpasses that of NiFe/NF, indicating effective interaction with the electrolyte and expedited release of *in-situ* generated bubbles.

The comparison of C_{dl} across different media, which is directly correlated with the electrochemical active surface area (ECSA), reveals that the ECSA of each catalyst remains nearly constant (Fig. S31). *Operando* Raman spectra indicate that the catalytically active phase for OER remains as γ-NiOOH in an alkaline natural seawater medium (Fig. S32). However, the overpotential required to achieve the same incremental current in alkaline seawater is markedly higher than that in 1.0 M KOH media. Given the pivotal impact of the microenvironment on catalytic performance, the intricate composition of anions in seawater can significantly perturb the catalytic microenvironment, thereby influencing the efficiency of OER [58,59]. This aspect has often been overlooked in prior studies of seawater electrolysis [9,60,61].

Finite element analysis (FEA) was performed using COMSOL Mutiphysics based on the Poisson-Nernst-Planck (PNP) model. For alkaline fresh water and alkaline simulated seawater, the system included hydrated hydroxide ions, potassium ions, and an additional 0.5 M of hydrated chloride ions with 0.5 M hydrated sodium ions, respectively. In the case of alkaline natural seawater, the components of standard seawater with concentrations higher than 10^{-5} M were considered, except for cations that precipitate under alkaline conditions (Table S9) [62]. As depicted in Fig. 6a, the presence of extra anions leads to a notable reduction in the concentration of hydrated hydroxide ions near the outer Helmholtz plane (OHP). The maximum hydroxide concentration near the OHP decreases from 10.72 M in alkaline fresh water media
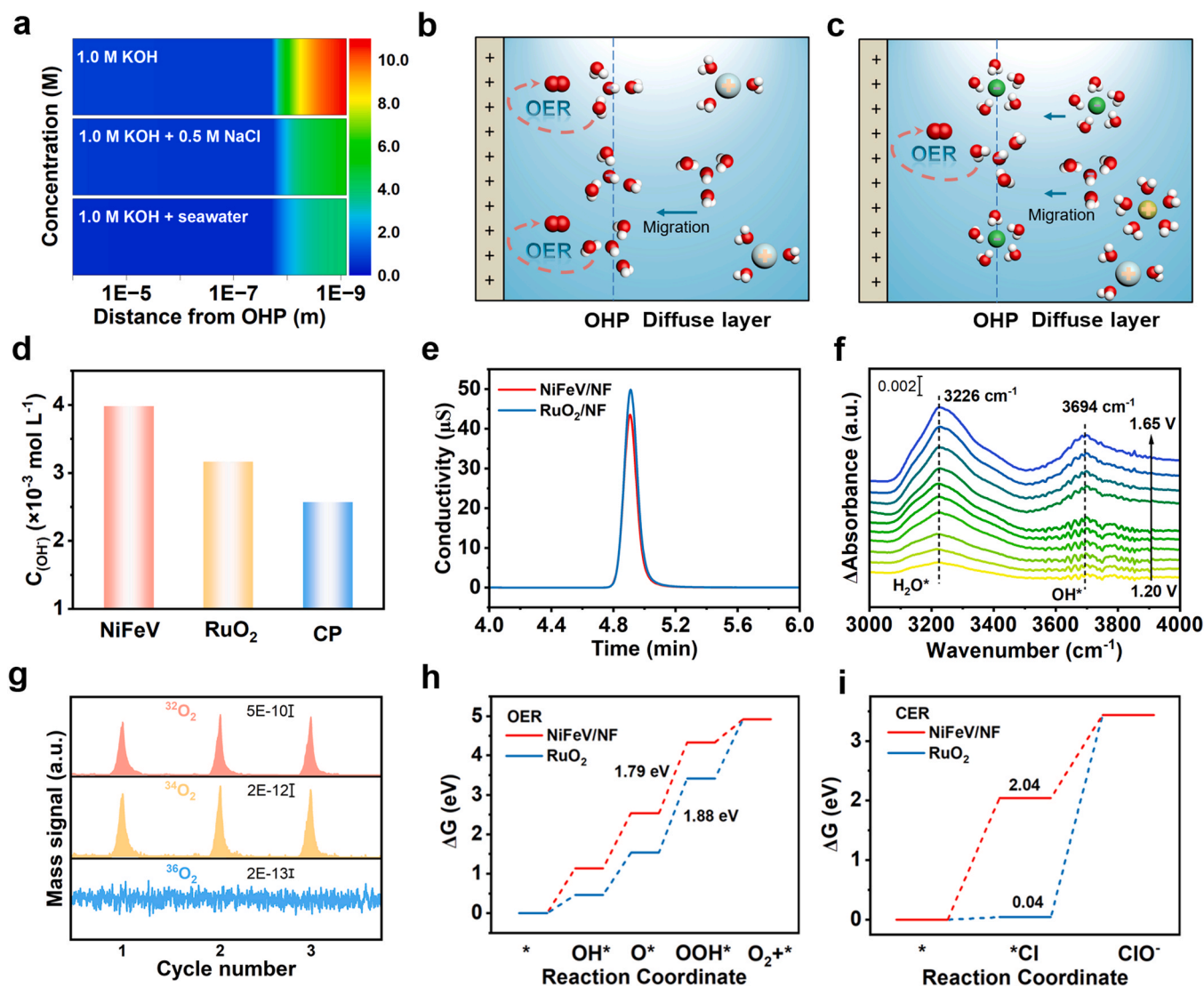
Fig. 6. Theoretical simulation and analysis. (a) The concentration of OH⁻ profiles over distance from OHP in different electrolytes. Schemata of double layer near anode in 1.0 M KOH (b) and alkaline natural seawater media (c) The color scheme for chemical representation: red for O, gray for H, cyan for K, green for Cl and yellow for Na. (d) Comparison of OH⁻ concentration on NiFeV and RuO$_2$ electrode. (e) Concentration of Cl⁻ determined by ion chromatography. (f) *In situ* ATR-SEIRAS of NiFeV/NF. (g) DEMS signals of O$_2$ product for NiFeV/NF. (h) Calculated free energy diagram of AEM mechanism. (i) Calculated free energy diagram for CER.

(pH = 13.8) to 3.93 M in alkaline natural seawater media (pH = 13.6) under the same bias. The influence of bulk solution pH is negligible (Fig. S33). Furthermore, as the current density increases, the hydroxide concentration near the OHP decreases rapidly, while the concentration of hydrated chloride ions steadily increases in both alkaline simulated seawater and alkaline natural seawater (Fig. S34). The FEA also indicates that the concentration of hydrated hydroxide near the OHP is higher and remains constant with increasing current in the Cl⁻-free medium (Fig. S35). This observation suggests a strong competitive adsorption between hydrated chloride ions and hydrated hydroxide ions at the OHP, which significantly hampers the mass transfer of hydrated hydroxide ions. Particularly at high current densities, the presence of relatively inert hydrated chloride ions on the OHP impedes the replenishment of hydrated hydroxide ions (Fig. 6b and Fig. 6c). The aggregation effect of other anions present in natural seawater was also examined and found to produce similar cathodic effects (Fig. S36). These findings underscore that the hindered mass transfer of hydrated hydroxide ions constitutes a pivotal factor in the decay of OER activity in alkaline seawater.

Based on the aforementioned analysis, a catalyst exhibiting a high

concentration of hydroxide and a low concentration of chloride ions on its surface is conducive to achieving heightened activity and selectivity in alkaline seawater. To further investigate this aspect, we utilized a reported method for electrode pH testing (Fig. S37) to assess the pH and chloride ion concentration on both NiFeV and commercial RuO$_2$ electrodes [40,63]. As illustrated in Fig. S38, the hydroxide concentration on the NiFeV electrode noticeably decreased upon transitioning from 1.0 M KOH to 1.0 M KOH + natural seawater, aligning with the FEA outcomes. Notably, within an alkaline natural seawater medium, the hydroxide concentration on the NiFeV electrode was 1.26 times greater than that on commercial RuO$_2$ (Fig. 6d). Furthermore, ion chromatography results displayed a lower chloride ion concentration on the NiFeV electrode compared to RuO$_2$ (Fig. 6e). This suggests that the NiFeV electrode effectively enriches hydroxide ions while inhibiting chloride ion adsorption, thus maintaining exceptional activity and selectivity in alkaline seawater.

In situ ATR-SEIRAS measurements conducted in 1.0 M KOH were employed to determine the OER reaction intermediates (Fig. 6f). The absorption band peaking at 3694 cm⁻¹ was attributed to OH* [64,65]. Notably, the peak intensity significantly increases upon reaching a

potential of 1.40 V (vs. RHE), indicating the generation of a substantial number of reaction intermediates. To discern the mechanism of oxygen generation for the NiFeV electrode, tests were conducted in both 1.0 M KOH and 1.0 M TMAOH. Similar OER activities observed in both media indicated the absence of O_2^{2-} intermediates. Furthermore, the NiFeV electrode exhibited an evident pH-independent feature (Fig. S39). To further explore this phenomenon, *operando* differential electrochemical mass spectrometry (DEMS) measurements using O^{18} isotope labeling were performed. As depicted in Fig. 6**g** and Fig. S40, the absence of $^{36}O_2$ signals on NiFeV electrode, coupled with a $^{34}O_2/^{32}O_2$ ratio lower than 0.5 %, unequivocally manifests the effective suppression of the LOM mechanism. Taken together, these compelling lines of evidence strongly suggest that the OER at the NiFeV electrode is more likely to proceed through the AEM mechanism.

Expanding upon *operando* Raman results and the investigation of the reaction pathway, DFT calculation was conducted to analyzed the impact of V doping on the OER process. The transformation of $Ni(OH)_2$ to NiOOH is achieved by stepwise electrochemical dehydrogenation. Hence, the deprotonation energy barrier of the $NiFe(OH)_2$ and NiFeV $(OH)_2$ pre-catalysts was calculated to clarify their ability to produce NiOOH. The energy for deprotonation reaction in $NiFe(OH)_2$ is 2.31 eV. When the V atoms are introduced, the free energy difference drops to 1.99 eV for $NiFeV(OH)_2$, which suggests that the transformation from $NiFeV(OH)_2$ to NiFeVOOH is thermodynamically more favourable (Fig. S41). Additionally, the influence of changes in the coordination environment resulting from V doping on the deprotonation process was analyzed. The deprotonation energy of the representative Ni-OH in $NiFeV(OH)_2$ (0.35 eV) was significantly lower than that in $NiFe(OH)_2$ (2.73 eV). Furthermore, the partial density of states (pDOS) of the metal center was assessed, revealing a shift in the d-band center of NiFeVOOH towards higher energy levels (Fig. S42). This shift results in an increased affinity for oxygen intermediates, potentially enhancing the catalytic efficiency of the OER. To further validate the aforementioned speculation, DFT + U calculations were conducted to construct a free energy diagram of the OER. Optimized structure models were presented in Fig. S43. As depicted in Fig. 6**h**, the generation of OOH* was identified as the potential-determining step (PDS) with the free energy barriers of 1.79 eV (1.88 eV for RuO_2) for the AEM pathway. Conversely, the deprotonation of OH* to generate O* represented the PDS via LOM (Fig. S44). The calculated free energy barrier of 2.38 eV for LOM was notably higher than that for AEM. This finding is consistent with the experimental indication that NiFeV is inclined to follow the AEM mechanism. The robust lattice oxygen guarantees the sustained functionality of the catalyst over extended periods.

Furthermore, the CER was explored to gain insights into the superior OER selectivity observed in alkaline seawater (>99 %). It was revealed that the formation of Cl* on NiFeV necessitates a high energy barrier of 2.04 eV. The projected density of states illustrates that the d orbitals of metals overlap the oxygen 2p orbitals better than the chlorine 3p orbitals (Fig. 6**i**, Fig. S45 **and** Fig. S46). In contrast, RuO_2 exhibited robust chloride ions adsorption, leading to significant OER performance reduction due to active site occupation by chloride ions. In summary, through a combination of experiments and theoretical simulations, it is evident that NiFeV/NF displays moderate oxygen species affinity and a low OER energy barrier, resulting in enhanced OER activity while mitigating anion aggregation limitations in seawater electrolytes. Moreover, the high energy barrier for chloride ion adsorption ensures robust OER selectivity.

3.6. Expansion of the NiFeX/NF system

The straightforward preparation method, involving only impregnation and calcination steps, demonstrates potential for industrial-scale catalyst production. To extend its applicability, we introduced various transition-metals (Mn, Co, Cu, Zn, Mo, W) and rare-earth metals (La, Ce) to modify the catalytic property of NiFe catalysts. As depicted in

Fig. S47, a range of NiFeX/NF (X = Mn, Co, Cu, Zn, Mo, W, La and Ce) catalysts were prepared using our impregnation method. SEM images and corresponding EDS mapping confirmed the successful incorporation of elements (Figs. S48-S55). OER catalytic activity was evaluated in both 1.0 M KOH and 1.0 M alkaline natural seawater (Fig. S56). The data underscored that the introduction of variable-valence metals enhanced OER activity. Notably, NiFeW/NF and NiFeCe/NF displayed exceptional water oxidation activity in both media, requiring only 380 mV and 371 mV overpotentials, respectively, to achieve 1.5 A cm^{-2} OER activity in 1.0 M KOH.

Moreover, these catalysts exhibited outstanding performance in alkaline natural seawater electrolyte, exceeding 1.0 A cm^{-2} at overpotentials of <480 mV, indicating great potential for industrial-scale seawater splitting at high current densities. Given that NiOOH is the pivotal catalytically active phase in our system, the doping of variable-valence metals is expected to expedite the dynamic conversion between Ni^{2+} and $Ni^{3+\delta}$ due to their exceptional electron transfer capability. To illustrate this effect, we investigated the impact of metal valence variability using W and Zn as representative examples. Cyclic voltammetry results reveal that W doping accelerates the oxidation of Ni^{2+} and the reduction of $Ni^{3+\delta}$ in comparison to Zn doping (Fig. S57). Concurrently, *operando* Raman spectra demonstrate that γ-NiOOH begins to form at 1.40 V (vs. RHE) on NiFeW/NF and at 1.42 V (vs. RHE) on NiFeZn/NF. Following complete oxidation at 1.40 V (vs. RHE) and 1.42 V (vs. RHE) over a 10-minute interval for NiFeW/NF and NiFeZn/NF, respectively, the generated γ-NiOOH is subsequently reduced upon application of potentials at 1.20 V (vs. RHE) and 1.22 V (vs. RHE). Notably, the Raman spectra reveal a significant reduction in γ-NiOOH on the NiFeW/NF surface within 60 seconds, while the quantity of γ-NiOOH on NiFeZn remains relatively constant. Moreover, the reduction rate of γ-NiOOH on the NiFeW/NF surface is notably faster than that of NiFeZn/NF within a 600-second timeframe (Fig. S58). This corroborates that the strategy of variable-valence metal doping effectively expedites the redox cycle of the Ni species, offering novel insights for the design of advanced OER catalysts.

4. Conclusions

In conclusion, we have successfully manipulated the redox cycle of Ni species by leveraging V as a structural and electronic regulator through a straightforward and scalable impregnation method. The incorporation of V expedites the formation kinetics of the active phase NiOOH and optimizes OH* adsorption, resulting in superior OER activity. The synergy of FEA and DFT calculations demonstrates that the NiFeV/NF effectively circumvents competitive chlorine oxidation, owing to its diminished propensity for chlorine adsorption and robust capacity to enrich surface hydroxide. Benefiting from these virtues, NiFeV/NF exhibits remarkable OER activity in both alkaline water and seawater, maintaining robust performance over extended periods even at industrial scale current density. In the context of an MEA electrolyzer, employing NiFeV/NF as an anode enables the production of 17.3 L and 2.0 L of H_2 per hour within 3.0 V for alkaline water and natural seawater splitting, respectively. This enhanced strategy is transferable to other earth-abundant metals and holds significant promise for realizing sustainable large-scale hydrogen production from seawater.

CRediT authorship contribution statement

Hao Zhang: Writing – review & editing, Methodology. **Lingling Xi:** Data curation. **Yong Wang:** Writing – review & editing, Supervision, Methodology, Funding acquisition, Formal analysis, Conceptualization. **Menghui Qi:** Writing – original draft, Methodology, Data curation. **Minkai Qin:** Methodology, Formal analysis, Data curation. **Hao Wang:** Investigation, Data curation. **Binbin Lin:** Investigation, Data curation. **Jiadong Chen:** Supervision, Data curation. **Xiaoyun Shi:** Data curation. **Xiangbowen Du:** Data curation. **Shanjun Mao:** Methodology, Funding

acquisition. **Jingpeng Zhao:** Data curation.

Declaration of Competing Interest

The authors declare no competing financial interest.

Data Availability

No data was used for the research described in the article.

Appendix A. Supporting information

Supplementary data associated with this article can be found in the online version at doi:10.1016/j.apcatb.2024.124259.

References

[1] N.S. Lewis, D.G. Nocera, Powering the planet: chemical challenges in solar energy utilization, Proc. Natl. Acad. Sci. U. S. A. 103 (2006) 15729–15735.

[2] J.A. Turner, Sustainable hydrogen production, Science 305 (2004) 972–974.

[3] X. Bao, Y. Gong, Y. Chen, H. Zhang, Z. Wang, S. Mao, L. Xie, Z. Jiang, Y. Wang, Carbon vacancy defect-activated Pt cluster for hydrogen generation, J. Mater. Chem. A 7 (2019) 15364–15370.

[4] F.-Y. Chen, Z.-Y. Wu, Z. Adler, H. Wang, Stability challenges of electrocatalytic oxygen evolution reaction: from mechanistic understanding to reactor design, Joule 5 (2021) 1704–1731.

[5] S. Stiber, N. Sata, T. Morawietz, S.A. Ansar, T. Jahnke, J.K. Lee, A. Bazylak, A. Fallisch, A.S. Gago, K.A. Friedrich, A high-performance, durable and low-cost proton exchange membrane electrolyser with stainless steel components, Energy Environ. Sci. 15 (2022) 109–122.

[6] X. Zheng, Y. Chen, X. Bao, S. Mao, R. Fan, Y. Wang, In situ formed bimetallic carbide Ni$_6$Mo$_6$C nanodots and NiMoO$_x$ nanosheet array hybrids anchored on carbon cloth: Efficient and flexible self-supported catalysts for hydrogen evolution, ACS Catal. 10 (2020) 11634–11642.

[7] L. Gao, S. Yoshikawa, Y. Iseri, S. Fujimori, S. Kanae, An economic assessment of the global potential for seawater desalination to 2050, Water 9 (2017) 763.

[8] H. Xie, Z. Zhao, T. Liu, Y. Wu, C. Lan, W. Jiang, L. Zhu, Y. Wang, D. Yang, Z. Shao, A membrane-based seawater electrolyser for hydrogen generation, Nature 612 (2022) 673–678.

[9] J. Guo, Y. Zheng, Z. Hu, C. Zheng, J. Mao, K. Du, M. Jaroniec, S.-Z. Qiao, T. Ling, Direct seawater electrolysis by adjusting the local reaction environment of a catalyst, Nat. Energy 8 (2023) 264–272.

[10] S. Dresp, F. Dionigi, M. Klingenhof, T. Merzdorf, H. Schmies, J. Drnec, A. Poulain, P. Strasser, Molecular understanding of the impact of saline contaminants and alkaline pH on NiFe layered double hydroxide oxygen evolution catalysts, ACS Catal. 11 (2021) 6800–6809.

[11] F. Dionigi, T. Reier, Z. Pawolek, M. Gliech, P. Strasser, Design criteria, operating conditions, and nickel-iron hydroxide catalyst materials for selective seawater electrolysis, ChemSusChem 9 (2016) 962–972.

[12] S. Dresp, F. Dionigi, S. Loos, J. Ferreira de Araujo, C. Spöri, M. Gliech, H. Dau, P. Strasser, Direct electrolytic splitting of seawater: activity, selectivity, degradation, and recovery studied from the molecular catalyst structure to the electrolyzer cell level, Adv. Energy Mater. 8 (2018) 1800338.

[13] B. Zhang, J. Wang, B. Wu, X.W. Guo, Y.J. Wang, D. Chen, Y.C. Zhang, K. Du, E. E. Oguzie, X.L. Ma, Unmasking chloride attack on the passive film of metals, Nat. Commun. 9 (2018) 2559.

[14] T. Cui, J. Chi, J. Zhu, X. Sun, J. Lai, Z. Li, L. Wang, Tuning the size and chemisorption of FeP$_4$ by trace Ru doping for hydrazine-assisted hydrogen evolution in seawater at large-current-density, Appl. Catal. B 319 (2022) 121950.

[15] J. Zhao, H. Guo, Q. Zhang, Y. Li, L. Gu, R. Song, Trace Ru atoms implanted into a Ni/Fe-based oxalate solid-solution-like with high-indexed facets for energy-saving overall seawater electrolysis assisted by hydrazine, Appl. Catal. B 325 (2023) 122354.

[16] H. You, D. Wu, D. Si, M. Cao, F. Sun, H. Zhang, H. Wang, T.F. Liu, R. Cao, Monolayer NiIr-layered double hydroxide as a long-lived efficient oxygen evolution catalyst for seawater splitting, J. Am. Chem. Soc. 144 (2022) 9254–9263.

[17] J. Wang, J. Chen, J. Zhang, Q. Gao, B. Han, R. Sun, C. Zhou, Z. Cai, Glassy state hydroxide materials for oxygen evolution electrocatalysis, Small (2024) e2312168.

[18] Y. Zhao, D.P. Adiyeri Saseendran, C. Huang, C.A. Triana, W.R. Marks, H. Chen, H. Zhao, G.R. Patzke, Oxygen evolution/reduction reaction catalysts: From in situ monitoring and reaction mechanisms to rational design, Chem. Rev. 123 (2023) 6257–6358.

[19] R. Subbaraman, D. Tripkovic, K.C. Chang, D. Strmcnik, A.P. Paulikas, P. Hirunsit, M. Chan, J. Greeley, V. Stamenkovic, N.M. Markovic, Trends in activity for the water electrolyser reactions on 3d M(Ni,Co,Fe,Mn) hydr(oxy)oxide catalysts, Nat. Mater. 11 (2012) 550–557.

[20] X. Du, M. Qi, Y. Wang, From atomic-level synthesis to device-scale reactors: A multiscale approach to water electrolysis, Acc. Chem. Res 57 (2024) 1298–1309.

[21] Z.P. Wu, H. Zhang, S. Zuo, Y. Wang, S.L. Zhang, J. Zhang, S.Q. Zang, X.W. Lou, Manipulating the local coordination and electronic structures for efficient electrocatalytic oxygen evolution, Adv. Mater. 33 (2021) e2103004.

[22] X. Xu, F. Song, X. Hu, A nickel iron diselenide-derived efficient oxygen-evolution catalyst, Nat. Commun. 7 (2016) 12324.

[23] L. Yu, Q. Zhu, S. Song, B. McElhenny, D. Wang, C. Wu, Z. Qin, J. Bao, Y. Yu, S. Chen, Z. Ren, Non-noble metal-nitride based electrocatalysts for high-performance alkaline seawater electrolysis, Nat. Commun. 10 (2019) 5106.

[24] Y. Wang, P. Yang, Y. Gong, D. Liu, S. Liu, W. Xiao, Z. Xiao, Z. Li, Z. Wu, L. Wang, Amorphous high-valence Mo-doped NiFeP nanospheres as efficient electrocatalysts for overall water-splitting under large-current density, Chem. Eng. J. 468 (2023) 143833.

[25] W.-J. Yin, B. Weng, J. Ge, Q. Sun, Z. Li, Y. Yan, Oxide perovskites, double perovskites and derivatives for electrocatalysis, photocatalysis, and photovoltaics, Energy Environ. Sci. 12 (2019) 442–462.

[26] J.L. Fillol, Z. Codola, I. Garcia-Bosch, L. Gomez, J.J. Pla, M. Costas, Efficient water oxidation catalysts based on readily available iron coordination complexes, Nat. Chem. 3 (2011) 807–813.

[27] J. Wang, M.-I. Jamesh, Q. Gao, B. Han, R. Sun, H.-Y. Hsu, C. Zhou, Z. Cai, Semimetallic hydroxide materials for electrochemical water oxidation, Sci. China Mater. 67 (2024) 1551–1558.

[28] M. Gorlin, P. Chernev, J. Ferreira de Araujo, T. Reier, S. Dresp, B. Paul, R. Krahnert, H. Dau, P. Strasser, Oxygen evolution reaction dynamics, faradaic charge efficiency, and the active metal redox states of Ni-Fe oxide water splitting electrocatalysts, J. Am. Chem. Soc. 138 (2016) 5603–5614.

[29] R. Mehmood, W. Fan, X. Hu, J. Li, P. Liu, Y. Zhang, Z. Zhou, J. Wang, M. Liu, F. Zhang, Confirming high-valent iron as highly active species of water oxidation on the Fe, V-coupled bimetallic electrocatalyst: In situ analysis of x-ray absorption and Mossbauer spectroscopy, J. Am. Chem. Soc. 145 (2023) 12206–12213.

[30] N. Zhang, X. Feng, D. Rao, X. Deng, L. Cai, B. Qiu, R. Long, Y. Xiong, Y. Lu, Y. Chai, Lattice oxygen activation enabled by high-valence metal sites for enhanced water oxidation, Nat. Commun. 11 (2020) 4066.

[31] S. Niu, W.J. Jiang, Z. Wei, T. Tang, J. Ma, J.S. Hu, L.J. Wan, Se-doping activates FeOOH for cost-effective and efficient electrochemical water oxidation, J. Am. Chem. Soc. 141 (2019) 7005–7013.

[32] C. Huang, Q. Zhou, D. Duan, L. Yu, W. Zhang, Z. Wang, J. Liu, B. Peng, P. An, J. Zhang, L. Li, J. Yu, Y. Yu, The rapid self-reconstruction of Fe-modified Ni hydroxysulfide for efficient and stable large-current-density water/seawater oxidation, Energy Environ. Sci. 15 (2022) 4647–4658.

[33] Y. Bai, Y. Wu, X. Zhou, Y. Ye, K. Nie, J. Wang, M. Xie, Z. Zhang, Z. Liu, T. Cheng, C. Gao, Promoting nickel oxidation state transitions in single-layer NiFeB hydroxide nanosheets for efficient oxygen evolution, Nat. Commun. 13 (2022) 6094.

[34] M. Qin, J. Chen, X. Zheng, M. Qi, R. Yang, S. Mao, Y. Wang, Operando deciphering the activity origins for potential-induced reconstructed oxygen-evolving catalysts, Appl. Catal. B 316 (2022) 121602.

[35] X. Zheng, M. Qin, S. Ma, Y. Chen, H. Ning, R. Yang, S. Mao, Y. Wang, Strong oxide-support interaction over IrO$_2$/V$_2$O$_5$ for efficient pH-universal water splitting, Adv. Sci. 9 (2022) e2104636.

[36] Y.-F. Li, A. Selloni, Mechanism and activity of water oxidation on selected surfaces of pure and Fe-doped NiO$_x$, ACS Catal. 4 (2014) 1148–1153.

[37] L. Zhuang, J. Li, K. Wang, Z. Li, M. Zhu, Z. Xu, Structural buffer engineering on metal oxide for long-term stable seawater splitting, Adv. Funct. Mater. 32 (2022) 2201127.

[38] M. Liu, Y. Pang, B. Zhang, P. De Luna, O. Voznyy, J. Xu, X. Zheng, C.T. Dinh, F. Fan, C. Cao, F.P. de Arquer, T.S. Safaei, A. Mepham, A. Klinkova, E. Kumacheva, T. Filleter, D. Sinton, S.O. Kelley, E.H. Sargent, Enhanced electrocatalytic CO$_2$ reduction via field-induced reagent concentration, Nature 537 (2016) 382–386.

[39] J. Gu, S. Liu, W. Ni, W. Ren, S. Haussener, X. Hu, Modulating electric field distribution by alkali cations for CO$_2$ electroreduction in strongly acidic medium, Nat. Catal. 5 (2022) 268–276.

[40] X. Li, H. Zhang, Q. Hu, W. Zhou, J. Shao, X. Jiang, C. Feng, H. Yang, C. He, Amorphous NiFe oxide-based nanoreactors for efficient electrocatalytic water oxidation, Angew. Chem. Int. Ed. 62 (2023) e202300478.

[41] J.E. Huang, F. Li, A. Ozden, A.S. Rasouli, F.P.G. de Arquer, S. Liu, S. Zhang, M. Luo, X. Wang, Y. Lum, Y. Xu, K. Bertens, R.K. Miao, C.-T. Dinh, D. Sinton, E.H. Sargent, CO$_2$ electrolysis to multicarbon products in strong acid, Science 372 (2021) 1074–1078.

[42] P. Liu, B. Chen, C. Liang, W. Yao, Y. Cui, S. Hu, P. Zou, H. Zhang, H.J. Fan, C. Yang, Tip-Enhanced Electric Field: A new mechanism promoting mass transfer in oxygen evolution reactions, Adv. Mater. 33 (2021) e2007377.

[43] M. Qin, R. Fan, J. Chen, H. Wang, X. Zheng, S. Mao, R. Du, Y. Wang, Elucidating electrocatalytic mechanism for large-scale cycloalkanol oxidation integrated with hydrogen evolution, Chem. Eng. J. 442 (2022) 136264.

[44] B. Zhang, Z. Wu, W. Shao, Y. Gao, W. Wang, T. Ma, L. Ma, S. Li, C. Cheng, C. Zhao, Interfacial atom-substitution engineered transition-metal hydroxide nanofibers

with high-valence Fe for efficient electrochemical water oxidation, Angew. Chem. Int. Ed. 61 (2022) e202115331.

[45] Z. Li, Y. Zhou, M. Xie, H. Cheng, T. Wang, J. Chen, Y. Lu, Z. Tian, Y. Lai, G. Yu, High-density cationic defects coupling with local alkaline-enriched environment for efficient and stable water oxidation, Angew. Chem. Int. Ed. 62 (2023) e202217815.

[46] P. Acharya, R.H. Manso, A.S. Hoffman, S.I.P. Bakovic, L. Kékedy-Nagy, S.R. Bare, J. Chen, L.F. Greenlee, Fe coordination environment, Fe-incorporated $Ni(OH)_2$ phase, and metallic core are key structural components to active and stable nanoparticle catalysts for the oxygen evolution reaction, ACS Catal. 12 (2022) 1992–2008.

[47] J. Wang, Y. Li, T. Xu, J. Zheng, K. Xiao, B. Sun, M. Ge, X. Yuan, C. Zhou, Z. Cai, Nanoporous nickel cathode with an electrostatic chlorine-resistant surface for industrial seawater electrolysis hydrogen production, Inorg. Chem. 63 (2024) 5773–5778.

[48] B. Lin, J. Chen, R. Yang, S. Mao, M. Qin, Y. Wang, Multi-hierarchical cobalt-based electrocatalyst towards high rate H_2 production, Appl. Catal. B 316 (2022) 121666.

[49] R. d'Amore-Domenech, T.J. Leo, Sustainable hydrogen production from offshore marine renewable farms: Techno-energetic insight on seawater electrolysis technologies, ACS Sustain. Chem. Eng. 7 (2019) 8006–8022.

[50] M.W. Louie, A.T. Bell, An investigation of thin-film Ni-Fe oxide catalysts for the electrochemical evolution of oxygen, J. Am. Chem. Soc. 135 (2013) 12329–12337.

[51] Y.J. Wu, J. Yang, T.X. Tu, W.Q. Li, P.F. Zhang, Y. Zhou, J.F. Li, J.T. Li, S.G. Sun, Evolution of cationic vacancy defects: A motif for surface restructuration of OER precatalyst, Angew. Chem. Int. Ed. 60 (2021) 26829–26836.

[52] D. Zhou, S. Wang, Y. Jia, X. Xiong, H. Yang, S. Liu, J. Tang, J. Zhang, D. Liu, L. Zheng, Y. Kuang, X. Sun, B. Liu, NiFe hydroxide lattice tensile strain: enhancement of adsorption of oxygenated intermediates for efficient water oxidation catalysis, Angew. Chem. Int. Ed. 58 (2019) 736–740.

[53] B.S. Yeo, A.T. Bell, In situ Raman study of nickel oxide and gold-supported nickel oxide catalysts for the electrochemical evolution of oxygen, J. Phys. Chem. C 116 (2012) 8394–8400.

[54] B.J. Trzesniewski, O. Diaz-Morales, D.A. Vermaas, A. Longo, W. Bras, M.T. Koper, W.A. Smith, In situ observation of active oxygen species in Fe-containing Ni-based oxygen evolution catalysts: the effect of pH on electrochemical activity, J. Am. Chem. Soc. 137 (2015) 15112–15121.

[55] L. Peng, N. Yang, Y. Yang, Q. Wang, X. Xie, D. Sun-Waterhouse, L. Shang, T. Zhang, G.I.N. Waterhouse, Atomic cation-vacancy engineering of NiFe-layered double hydroxides for improved activity and stability towards the oxygen evolution reaction, Angew. Chem. Int. Ed. 60 (2021) 24612–24619.

[56] T. Reier, H.N. Nong, D. Teschner, R. Schlögl, P. Strasser, Electrocatalytic oxygen evolution reaction in acidic environments-reaction mechanisms and catalysts, Adv. Energy Mater. 7 (2017) 160275.

[57] H.B. Tao, Y. Xu, X. Huang, J. Chen, L. Pei, J. Zhang, J.G. Chen, B. Liu, A general method to probe oxygen evolution intermediates at operating conditions, Joule 3 (2019) 1498–1509.

[58] V.R. Stamenkovic, D. Strmcnik, P.P. Lopes, N.M. Markovic, Energy and fuels from electrochemical interfaces, Nat. Mater. 16 (2016) 57–69.

[59] T. Ma, W. Xu, B. Li, X. Chen, J. Zhao, S. Wan, K. Jiang, S. Zhang, Z. Wang, Z. Tian, Z. Lu, L. Chen, The critical role of additive sulfate for stable alkaline seawater oxidation on nickel-based electrodes, Angew. Chem. Int. Ed. 60 (2021) 22740–22744.

[60] S. Dresp, F. Dionigi, M. Klingenhof, P. Strasser, Direct electrolytic splitting of seawater: opportunities and challenges, ACS Energy Lett. 4 (2019) 933–942.

[61] X. Xiao, L. Yang, W. Sun, Y. Chen, H. Yu, K. Li, B. Jia, L. Zhang, T. Ma, Electrocatalytic water splitting: from harsh and mild conditions to natural seawater, Small 18 (2022) e2105830.

[62] F.J. Millero, R. Feistel, D.G. Wright, T.J. McDougall, The composition of standard seawater and the definition of the reference-composition salinity scale, Deep Sea Res. Part I Oceanogr. Res. Pap. 55 (2008) 50–72.

[63] G. Chen, H. Li, Y. Zhou, C. Cai, K. Liu, J. Hu, H. Li, J. Fu, M. Liu, CoS_2 needle arrays induced a local pseudo-acidic environment for alkaline hydrogen evolution, Nanoscale 13 (2021) 13604–13609.

[64] S. Zhu, X. Qin, Y. Yao, M. Shao, pH-Dependent hydrogen and water binding energies on platinum surfaces as directly probed through surface-enhanced infrared absorption spectroscopy, J. Am. Chem. Soc. 142 (2020) 8748–8754.

[65] X. Zheng, X. Shi, H. Ning, R. Yang, B. Lu, Q. Luo, S. Mao, L. Xi, Y. Wang, Tailoring a local acid-like microenvironment for efficient neutral hydrogen evolution, Nat. Commun. 14 (2023) 4209.